RESEARCH ARTICLE | MAY 27 2025

# A logic metastructure for register function implementation

Jia-Hao Zou ; Jun-Yang Sui ; Hai-Feng Zhang



*Appl. Phys. Lett.* 126, 213502 (2025)
https://doi.org/10.1063/5.0265284

Applied Physics Letters ARTICLE pubs.aip.org/aip/apl

# A logic metastructure for register function implementation

Cite as: Appl. Phys. Lett. **126**, 213502 (2025); doi: 10.1063/5.0265284
Submitted: 13 February 2025 · Accepted: 13 May 2025 ·
Published Online: 27 May 2025



Jia-Hao Zou, Jun-Yang Sui, and Hai-Feng Zhang[a)]

## AFFILIATIONS

College of Electronic and Optical Engineering & College of Flexible Electronics (Future Technology), Nanjing University of Posts and Telecommunications, Nanjing 210023, China

[a)]Author to whom correspondence should be addressed: hanlor@163.com and hanlor@njupt.edu.cn

## ABSTRACT

A coherent perfect absorption-based logic metastructure (LM) capable of register functionality is presented in the work. The unique one-dimensional layered architecture enables dual electromagnetic wave selectivity in both frequency and spatial angle domains within specific spectral ranges. The structure contains graphene layers as the tunable dielectric for the LM. By controlling the chemical potential of graphene, the incidence angle, and the phase difference of the coherent light, the coherent absorptivity of the LM can be changed accordingly. By establishing logic-level definitions for input/output signals, two distinct operational conditions that define logical relationships between inputs and outputs are derived. Under these dual operational modes, the LM achieves data registration across eight discrete addresses. The system employs clock signal synchronization to correlate outputs from both states with one serving as a block register that identifies the data block location and the other functioning as a data register outputting actual content. The combined output from both registers generates the complete physical address of stored data. This architectural design enables simultaneous 128-bit data registration ($8 \times 2 \times 8$), demonstrating the potential for high-density optical information processing applications.





Metastructures are artificially engineered periodic structures with unique physical, optical, and electromagnetic properties derived from the structural design at micro- or nanoscales.[1–4] Logic metastructures (LM) designed for logic operations are advanced optical components that manipulate light to execute logical operations.[5] Unlike traditional optical logic devices (OLDs),[6,7] LMs leverage specially engineered nanostructures to achieve precise control over the properties of light, such as phase,[8] polarization,[9] and space,[9] enabling ultra-fast and low-energy information processing. Zhao *et al.*[10] proposed the microwave LM, which can realize three basic logic operations under different input signals. An LM consisting of three split-ring resonators was designed by Bhattacharya *et al.*,[11] realizing binary computation operations in the terahertz (THz) frequency range. Zeng *et al.*[12] illustrated that an LM based on dual-channel gated high-density two-dimensional electronic gas can achieve high-speed logic modulation. These studies represent an advancement in all-optical logic computation, offering a conceptual framework for LM research. However, current implementations remain confined to employing LM for fundamental logic operations, without advancing toward application-specific photonic logic architectures. While the demonstration of photonic half-adder and half-subtractor based on LM has been accomplished,[13] the research of realizing register function based on LM is still blank.[14]

Herein, a coherent perfect absorption (CPA)-based LM that achieves photonic register functionality is presented. CPA leverages the principles of wave interference, where precise control of the phase differences and intensities of coherent electromagnetic waves (EWs) can lead to enhanced absorptivity, far exceeding that of single-port incidences.[15,16] Because of its ability to control the phase of EWs with high precision, CPA provides an efficient method for constructing LM.[13] Moreover, dual EWs selectivity in both the frequency and spatial angle domains within particular spectral ranges is made possible by the special one-dimensional layered design. Graphene layers are used as the adjustable dielectric in the LM. The coherent absorptivity ($A_c$) of the LM can be adjusted by varying the phase difference, the incidence angle, and the chemical potential of graphene. Logical relationships between inputs and outputs are obtained by defining logic levels of input/output signals under two separate operational conditions. The LM accomplishes register function over eight addresses under these two operating modes. To correlate the outputs from both states, the system uses clock signal synchronization with one acting as a block register that indicates the position of the data block and the other as a data register that outputs real

content. The full physical address of the stored data is produced by combining the output from the two registers.

As observable in Fig. 1(a), the given LM featuring the function of the register is a one-dimensional structure. It is composed of silicon dioxide ($SiO_2$),[17] germanium (Ge),[18] and graphene-based composite material (GCM), which are stacked in layers following a specific periodic. The GCM consists of a graphene layer[19] and $SiO_2$ interleaved, like $SiO_2$(graphene-$SiO_2$)$^N$, as shown in Fig. 1(b). The thickness of $SiO_2$ and Ge in the LM is defined as $d_A = 1\ \mu$m and $d_B = 2\ \mu$m, respectively. In this work, $SiO_2$ and Ge are regarded as ideal dielectric, and their refractive indices (RIs) are regarded as $n_A = 1.44$[17] and $n_B = 4$,[18] respectively. The conductivity $\sigma$ of graphene can be determined by $\sigma_{intra}$ and $\sigma_{inter}$, and the thickness of a single layer graphene is $d_g = 0.34$ nm.[19] The tangential RI of graphene can be expressed as[19]

$$n_g = \sqrt{1 + \frac{i\sigma}{\omega\varepsilon_0 d_g}}, \tag{1}$$

where $\omega$ and $\varepsilon_0$ severally correspond to the angular frequency and the vacuum permittivity constant, respectively. The properties of graphene can be changed by manipulating the chemical potential $\mu_c$. The GCM located in the middle of the LM is regulated by chemical potential $\mu_1$. For both sides of the LM, the two GCM layers are controlled by chemical potential $\mu_2$.

The LM is considered to be operated at different frequency points and different incidence angles, as shown in Fig. 1(c). The incidence angle of EWs 1 is defined as $\theta_1$, and the frequency of EWs 1 is about 161.5 or 168.5 THz. $\theta_2$ is regarded as the incidence angle of EWs 2, and the frequency of EWs 2 is 165 THz. To increase the electromagnetic response characteristics of the LM at different incidence angles, the EWs in this work are all incident in transverse magnetic (TM) modes.[20] (It is defined as the polarization mode where the electric field $E$ is in the $x$–$o$–$z$ plane and the magnetic field $H$ is along the $+y$-axis when EWs propagate along the $+z$-axis.) Under the condition, the transfer matrix of the LM can be given as[20]

$$\mathbf{M}_j = \begin{pmatrix} \cos(k_j d_j) & -\frac{i}{\eta_j}\sin(k_j d_j) \\ -i\eta_j \sin(k_j d_j) & \cos(k_j d_j) \end{pmatrix}, \tag{2}$$

where $k_j = \omega/cn_j$ is the wave vector and $j$ is signified by different dielectric layer materials A, B, and g. $\eta_j = (\varepsilon_0/\mu_0)^{1/2} n_j/\cos\theta_j$ is electromagnetic admittance, and $\theta_j$ is regarded as "$\arcsin(n_0 \sin\theta_i/n_j)$." $\varepsilon_0$ and $\mu_0$ represent the vacuum permittivity and vacuum permeability, respectively. $i$ is denoted by 1 or 2 and the value of $n_0$ is equal to 1 since the LM is exposed to air. The entire matrix ($\mathbf{M}$) of the proposed LM can be written as[20]

$$\mathbf{M} = \prod \mathbf{M}_j, \tag{3}$$

which can also be represented as a $2 \times 2$ matrix as[20]

$$\mathbf{M} = \begin{pmatrix} \mathbf{M}_{11} & \mathbf{M}_{12} \\ \mathbf{M}_{21} & \mathbf{M}_{22} \end{pmatrix}. \tag{4}$$

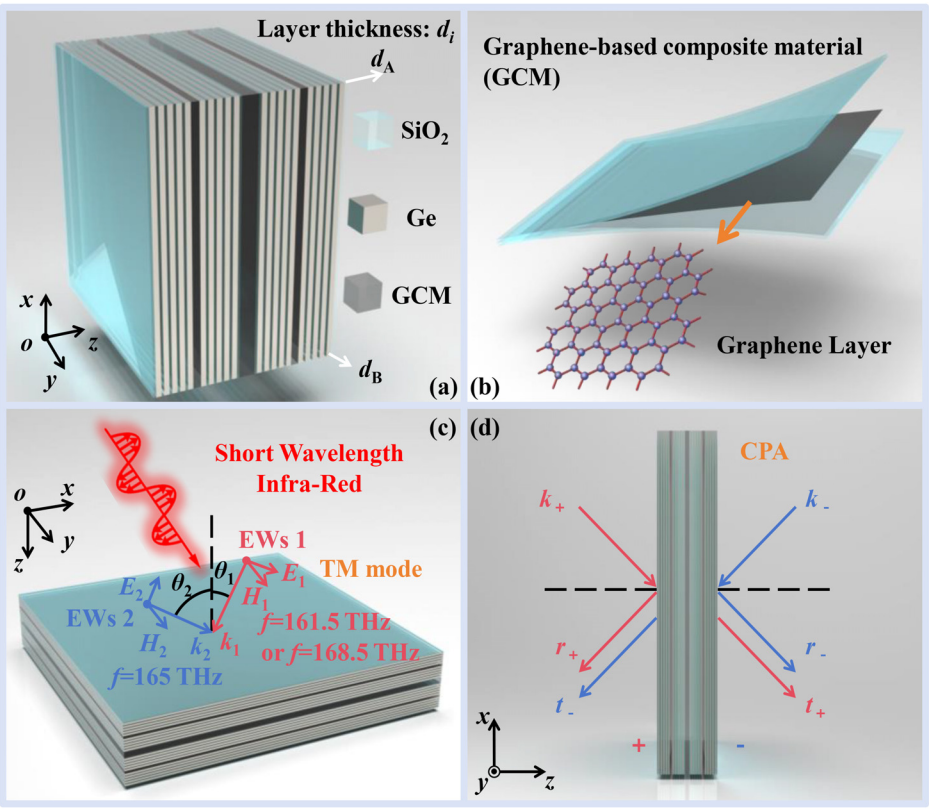


**FIG. 1.** Schematic diagram of the proposed LM. (a) The LM consists of different stacked dielectric layers. (b) GCM is composed of single-layer graphene and $SiO_2$ substrate based on the structure of (SiO$_2$Graphene)$^N$SiO$_2$. (c) Both EWs 1 (161.5 or 168.5 THz) and EWs 2 (165 THz) enter the LM in the TM mode. (d) Coherent EWs incident from positive and negative scales, respectively.

The following formula can be used to get the transmission coefficient ($t$) and the reflection coefficient ($r$):[20]

$$r = \frac{\eta_0(\mathbf{M}_{11} + \eta_0\mathbf{M}_{12}) - (\mathbf{M}_{21} + \eta_0\mathbf{M}_{22})}{\eta_0(\mathbf{M}_{11} + \eta_0\mathbf{M}_{12}) + (\mathbf{M}_{21} + \eta_0\mathbf{M}_{22})}, \tag{5}$$

$$t = \frac{2\eta_0}{\eta_0(\mathbf{M}_{11} + \eta_0\mathbf{M}_{12}) + (\mathbf{M}_{21} + \eta_0\mathbf{M}_{22})}. \tag{6}$$

The scattering matrix **S** can be utilized to explain this relationship of CPA presented in Fig. 1(d),[21]

$$\begin{pmatrix} O_+ \\ O_- \end{pmatrix} = \mathbf{S}\begin{pmatrix} I_+ \\ I_- \end{pmatrix} = \begin{pmatrix} r_+ & t_- \\ t_+ & r_- \end{pmatrix}\begin{pmatrix} I_+ \\ I_- \end{pmatrix}. \tag{7}$$

Because the proposed LM is a symmetrical structure, there are "$r = r_+ = r_-$" and "$t = t_+ = t_-$." "$r_+$," "$t_+$," "$r_-$," and "$t_-$," respectively, represent $r$ and $t$ of positive and negative scales. The observed EWs of both positive and negative scales ($O_+$ and $O_-$) are composed of the transmitted EWs from the opposite side and the reflected EWs from this side. $I_+$ and $I_-$ are defined as the intensities of incident EWs from positive and negative scales. Equation (10) can also be expressed as[21]

$$O_+ = r|I_+|e^{i\varphi_+} + t|I_-|e^{i\varphi_-}, \tag{8}$$

$$O_- = t|I_+|e^{i\varphi_+} + r|I_-|e^{i\varphi_-}, \tag{9}$$

where $\varphi_+$ and $\varphi_-$ are the phases of the EWs from positive and negative scales. The coherent absorptivity $A_c$ can be given as

$$A_c = 1 - \frac{|O_+|^2 + |O_-|^2}{|I_+|^2 + |I_-|^2}. \tag{10}$$

So, the formula for $A_c$ can be derived as[21]

$$A_c = 1 - (|t| - |r|)^2 - 2|t||r|\left(1 + \frac{2|I_+||I_-|\cos\Delta\varphi_1\cos\Delta\varphi_2}{|I_+|^2 + |I_-|^2}\right), \tag{11}$$

where $\Delta\varphi_1 = \mathrm{Arg}(t) - \mathrm{Arg}(r)$ and $\Delta\varphi_2 = \varphi_+ - \varphi_-$. $\mathrm{Arg}(t)$ and $\mathrm{Arg}(r)$ are regarded as the arguments of $t$ and $r$. Section I of the supplementary material provides a detailed analysis of the conditions for achieving CPA.

Figure 2 shows the curve of $A_c$ as the incidence angle changes in the cases of different $\Delta\varphi_2$, $\mu_1$, and $\mu_2$. Here, $\Delta\varphi_{12}$ represents $\Delta\varphi_2$ of coherent EWs 1, and $\Delta\varphi_{22}$ is defined as $\Delta\varphi_2$ of coherent EWs 2. To more intuitively show the effect of $\theta_1$, $\theta_2$, and other factors on $A_c$ of EWs 1 and EWs 2, conditions of forming high $A_c$ corresponding to Fig. 2 are presented in Table I. According to Table I, it can be found that $A_c$ of EWs 1 can be higher than 0.9 by regulating $\mu_1$, $\mu_2$, and $\Delta\varphi_{12}$ when $\theta_1$ is about 54° and 43.5°. In the case of $\theta_2 = 54°$ or $\theta_2 = 22.5°$, $A_c$ of EWs 2 can also exceed 0.9 through adjusting $\mu_1$, $\mu_2$, and $\Delta\varphi_{22}$, fixed at 180°. The LM forms high $A_c$ of EWs 1 and EWs 2 at these

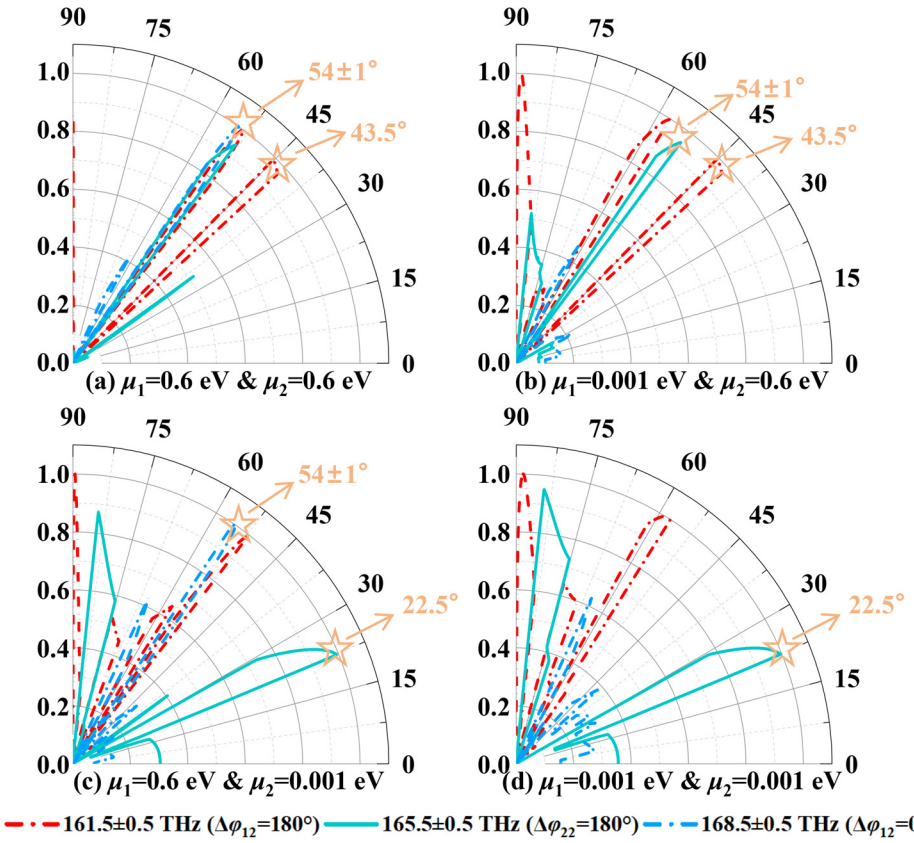


**FIG. 2.** The curve of $A_c$ as the incidence angle changes in the cases of different $\Delta\varphi_2$, $\mu_1$, and $\mu_2$. (a) In the case of $\mu_1 = 0.6$ eV and $\mu_2 = 0.6$ eV. (b) In the case of $\mu_1 = 0.001$ eV and $\mu_2 = 0.6$ eV. (c) In the case of $\mu_1 = 0.6$ eV and $\mu_2 = 0.001$ eV. (d) In the case of $\mu_1 = 0.001$ eV and $\mu_2 = 0.001$ eV.

**TABLE I.** The conditions of forming high peaks ($A_c > 0.9$) corresponding to Fig. 2.

| EWs 1 | | | | EWs 2 | | | |
|---|---|---|---|---|---|---|---|
| $\mu_1$ | $\mu_2$ | $\theta_1$ | $\Delta\varphi_{12}$ | $\mu_1$ | $\mu_2$ | $\theta_2$ | $\Delta\varphi_{22}$ |
| 0.6 eV | 0.6 eV | 54.5°/43.5° | 180° | 0.6 eV | 0.6 eV | 54.5° | 180° |
| 0.6 eV | 0.6 eV | 54.5° | 0° | 0.001 eV | 0.6 eV | 54.5° | 180° |
| 0.001 eV | 0.6 eV | 43.5° | 180° | 0.6 eV | 0.001 eV | 22.5° | 180° |
| 0.6 eV | 0.001 eV | 54.5° | 0°/180° | 0.001 eV | 0.001 eV | 22.5° | 180° |

specific incident angles and realizes angle selection. Moreover, the phase control of EWs also plays an important role in forming high $A_c$, and angle selection and phase control are the basis of spatial reuse in this work.[22] Section II of the supplementary material shows a solution for the problem of multi-spatial angle domains.

When $\theta_1$ is fixed at 54.5° or 43° and $\theta_2$ is fixed at 54.5° or 22.5°, the spectra under different $\mu_1$, $\mu_2$, and $\Delta\varphi_2$ are shown in Fig. 3. As can be seen in Figs. 3(a) and 3(b), the generation of sharp $A_c$ peaks of EWs 1 and EWs 2 is, respectively, affected by $\mu_1$ and $\mu_2$ when $\theta_1$ and $\theta_2$ are both fixed to 54.5°. In addition, the change of $\Delta\varphi_2$ (0° or 180°) only changes the frequency band in which the $A_c$ peaks of EWs 1 are generated, and has little effect on EWs 2. As shown in Table III, only $\Delta\varphi_{12}$ is considered as an adjustable point. When $\theta_2$ decreases to 22.5°, Fig. 3(c) displays that $A_c$ peaks of EWs 2 are still controlled by $\mu_2$, but the result is the exact opposite of Figs. 3(a) and 3(b). If $\theta_1$ drops to 43.5°, as shown in Fig. 3(d), $A_c$ peaks of EWs 1 are not controlled by $\mu_1$, but by $\mu_2$. Realizing spatial reuse can significantly improve the complexity of logical operation. The simulation software results in Sec. III of the supplementary material verify the accuracy of this working theory. Moreover, the error analyses of phase difference, incident angle, and chemical potential are proposed in Secs. IV and V of the supplementary material to analyze the robustness. This work can still achieve the planned functions within a limited error range, even though changing the chemical potential of graphene, the incidence angle, and the coherent light phase difference will diminish the absorption peak and shift its frequency point. The logical level corresponding to the chemical formula, phase difference, and incident angle of this work is represented by the uppercase of each physical quantity, respectively. Table II lists in detail the logical input ports involved.

To more clearly analyze the logical operations the LM can implement, the logic level of each physical signal is defined in Table III. $O_1$ and $O_2$ represent the output logic level of EWs 1 and EWs 2, respectively. When there is an absorption peak and $A_c$ is greater than 0.9, the output is expressed as "1" ($O_1$ = "1" or $O_2$ = "1"). If $A_c$ is less than 0.1, the output is regarded as "0" ($O_1$ = "0" or $O_2$ = "0"). For $M_1$ and $M_2$, higher values "0.6 eV" correspond to high logic level "1," and the level of "0" is defined as "0.001 eV." The logic level "1" for both $\Theta_1$ and $\Theta_2$ is regarded as the incident angle of 54.5°. The difference is that their low levels indicate the incidence angles of 43.5° and 22.5°, respectively. The $\Phi$ = "0" and $\Phi$ = "1" are defined as $\Delta\varphi_{12} = 0°$ and $\Delta\varphi_{12} = 180°$. As can be seen in Fig. 3, there are logical relationships between outputs ($O_1$ and $O_2$) and inputs ($M_1$, $M_2$, $\Theta_1$, and $\Theta_2$). To analyze the logical relationships more clearly, Table IV lists the corresponding truth tables. With the help of Sec. VI of the supplementary material, it can be seen that when $\Delta\varphi_2$ of EWs jumps between 0° and 180°, the $A_c$ curves hardly change in the case of $\theta = 43.5°$ or $\theta = 22.5°$. Therefore, whether $\Phi$ is 0 or 1, the response of EWs 1 and EWs 2 to the LM satisfies the truth table listed in Table IV, that is, satisfies the following equations:

$$O_1 = M_1\Theta_1 + M_2\overline{\Theta_1}, \tag{12}$$

$$O_2 = M_2\Theta_2 + \overline{M_2}\,\overline{\Theta_2}. \tag{13}$$

By combining the above-mentioned logical operations and controlling them, the function of the register under two different conditions can be realized, and their detailed truth tables are provided in Sec. VII of the supplementary material. When $\Theta_1$ is fixed as 1, Eqs. (12) and (13) are written as

$$O_1 = M_1, \tag{14}$$

$$O_2 = \overline{M_2 \oplus \Theta_2}. \tag{15}$$

If $M_2$ is controlled as the logical negation of $M_1$ ($M_2 = \sim M_1$), Eqs. (12) and (13) can be solved as

$$O_1 = \overline{M_1 \oplus \Theta_1}, \tag{16}$$

$$O_2 = \overline{M_2 \oplus \Theta_2}. \tag{17}$$

The flow charts corresponding to Eqs. (14)–(17) are shown in Fig. 4. Output $O_1$ satisfies the logical relation "$\Theta_1$ AND $M_1$," and the logical operations "$\Theta_2$ XNOR $M_1$" can represent the output $O_2$ (XNOR represents exclusive-NOR operation), as can be seen in Fig. 4(a), when $\Theta_1$ is fixed as 1. In the case of $M_2 = \sim M_1$, output $O_1$ satisfies "$\Theta_1$ XNOR $M_1$" and "$\Theta_2$ XNOR $M_1$" defines output $O_2$.

As can be seen in Fig. 5, if the two conditions ("$\Theta_1$ fixed as 1" and "$M_2 = \sim M_1$") can be controlled by a clock signal (it is defined in detail in Sec. VIII of the supplementary material), the registers of different time states can be divided into a block register and a data register. Both block register and data register output 4-bit results at the same time, which are $\Phi\Theta_2O_1O_2$ and $\Phi M_1O_2O_1$, respectively. The first three digits (marked blue in Fig. 5) of the 4-bit result represent the addresses. Unlike the block register, the fourth-bit (marked red in Fig. 5) output by the data register represents the real data, and the block register outputs the block number of the real data. In this work, the output of the arithmetic logic unit is temporarily stored in the electromagnetic signal through the special electromagnetic response of the LM. The internal memory can store the transmitted data by detecting electromagnetic signals. Detailed data transmission processes are shown in Fig. 6. Register number ($R$) is represented by the first two bits of the input signal. $R$ and third-bit output form the address of the fourth bit.

Figure 7 displays the flow chart of register function implementation when processing data with the same address as Fig. 6.

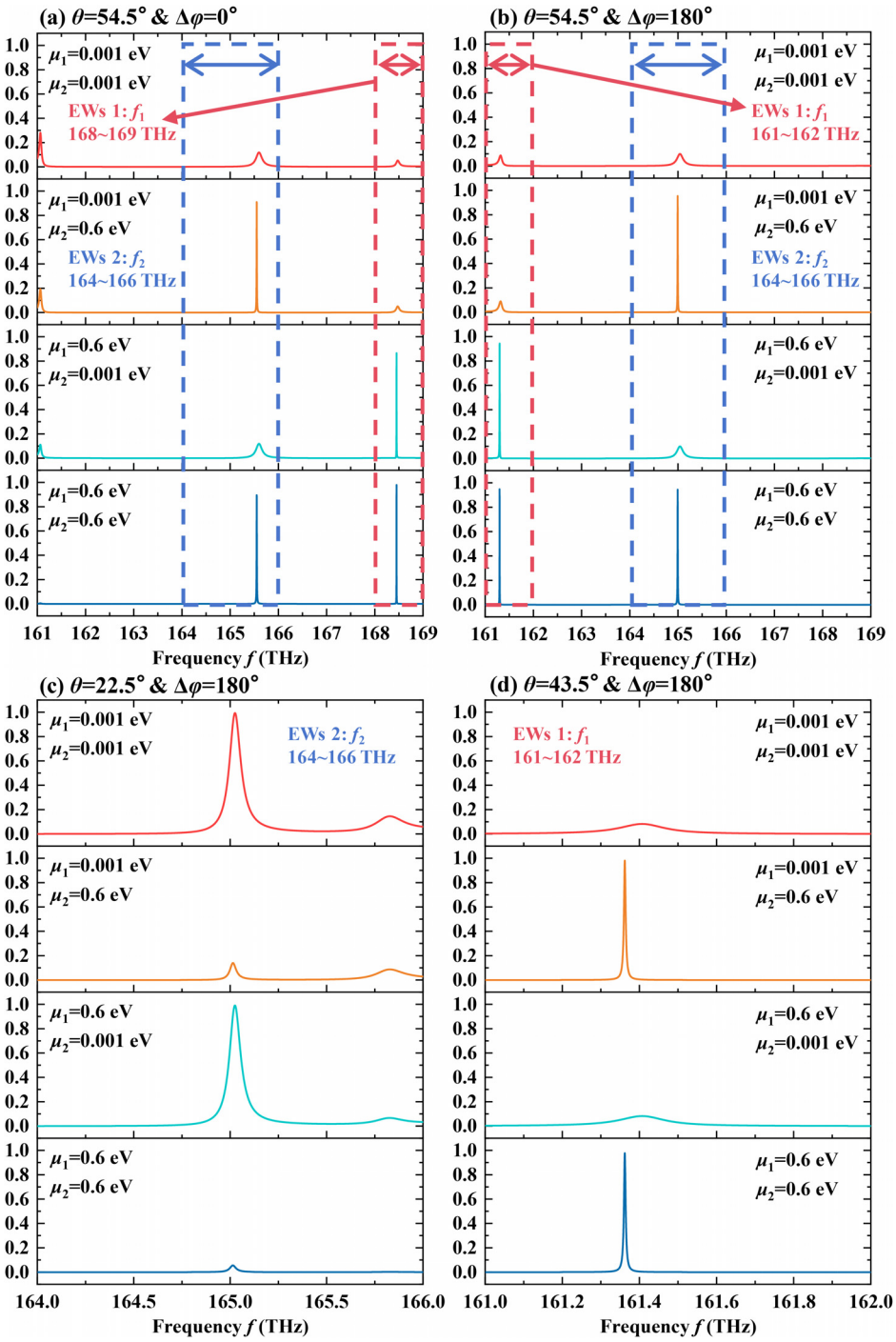


**FIG. 3.** The spectra under the different chemical potentials, phase difference ($\Delta\varphi$), and angle of incidence ($\theta$). (a) In the case of $\theta = 54.5°$ and $\Delta\varphi = 0°$. (b) In the case of $\theta = 54.5°$ and $\Delta\varphi = 180°$. (c) In the case of $\theta = 22.5°$ and $\Delta\varphi = 180°$. (d) In the case of $\theta = 43.5°$ and $\Delta\varphi = 180°$.

Figures 7(a) and 7(b) concretely show the data stored at "block 0" and "block 1," respectively. Each pixel represents one bit, and the surrounding binary numbers marked orange and green represent the absolute addresses corresponding to the data. As can be seen in Fig. 7(c), when the input is "$\Phi M_1 M_2 \Theta_1 \Theta_2 = 01011$," the output of the optical signal is

**TABLE II.** Logical input ports corresponding to physical signal.

| Physical signals | $\mu_1$ | $\mu_2$ | $\theta_1$ | $\theta_2$ | $\Delta\varphi_{12}$ |
|---|---|---|---|---|---|
| Logical input ports | $M_1$ | $M_2$ | $\Theta_1$ | $\Theta_2$ | $\Phi$ |

**TABLE III.** The logic level corresponding to each physical signal.

| Physical signals | $A_c$ | | $\mu_1$ and $\mu_2$ | | $\theta_1$ | | $\theta_2$ | | $\Delta\varphi_{12}$ | |
|---|---|---|---|---|---|---|---|---|---|---|
| Value | Less than 0.1 | Larger than 0.9 | 0.001 eV | 0.6 eV | 43.5° | 54.5° | 22.5° | 54.5° | 0° | 180° |
| Logic level | $O_1$ = "0"<br>$O_2$ = "0" | $O_1$ = "1"<br>$O_2$ = "1" | $M_1$ = "0"<br>$M_2$ = "0" | $M_1$ = "1"<br>$M_2$ = "1" | $\Theta_1$ = "0" | $\Theta_1$ = "1" | $\Theta_2$ = "0" | $\Theta_2$ = "1" | $\Phi$ = "0" | $\Phi$ = "1" |

**TABLE IV.** The truth tables corresponding to the logical relationships between outputs and inputs.

| EWs 1 | | | | EWs 2 | | | |
|---|---|---|---|---|---|---|---|
| INPUTS | | | OUTPUTS | INPUTS | | | OUTPUTS |
| $M_1$ | $M_2$ | $\Theta_1$ | $O_1$ | $M_1$ | $M_2$ | $\Theta_2$ | $O_2$ |
| 0 | | 1 | 0 | 0 | 1 | | 0 |
| 1 | | | 1 | 1 | | | 1 |
| | 0 | 0 | 0 | 0 | | 0 | 1 |
| | 1 | | 1 | 1 | | | 0 |

"$\Phi\Theta_2O_1O_2 = 0110$" according to the logic operations described above. Based on the process of block register, the address "011" in "block 0" is selected by the LM. When advancing to the data register process, if the input signal is "$\Phi M_1M_2\Theta_1\Theta_2 = 001X$," the absolute address of the real data in "block 0" is "011–001." The signal "X" input to $\Theta_1$ is regarded as the real data at this absolute address "011–001."

The signal-to-noise ratio (*SNR*) is used to evaluate the dependability of LM.[23] The *SNR* formula is written as[23]

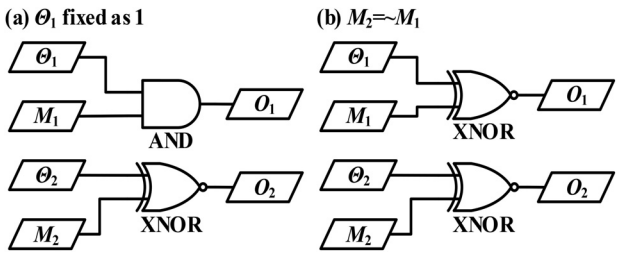


**FIG. 4.** The flow charts corresponding to logical operations for the register function. (a) $\Theta_1$ is fixed as 1. (b) $M_2$ is controlled as non-$M_1$.

$$SNR(dB) = 10log_{10}\left(\frac{A_1}{A_0}\right), \tag{18}$$

where the values of $A_c$ at an output value of "1" or "0" are represented individually by $A_1$ and $A_0$. "$SNR = 3$ dB" is considered to be the cutoff point between low and high *SNR*s. To systematically highlight the comparative advantages of this research, Table V provides a comprehensive comparison between our work and existing studies on OLDs. Unlike previous investigations primarily focused on fundamental logic

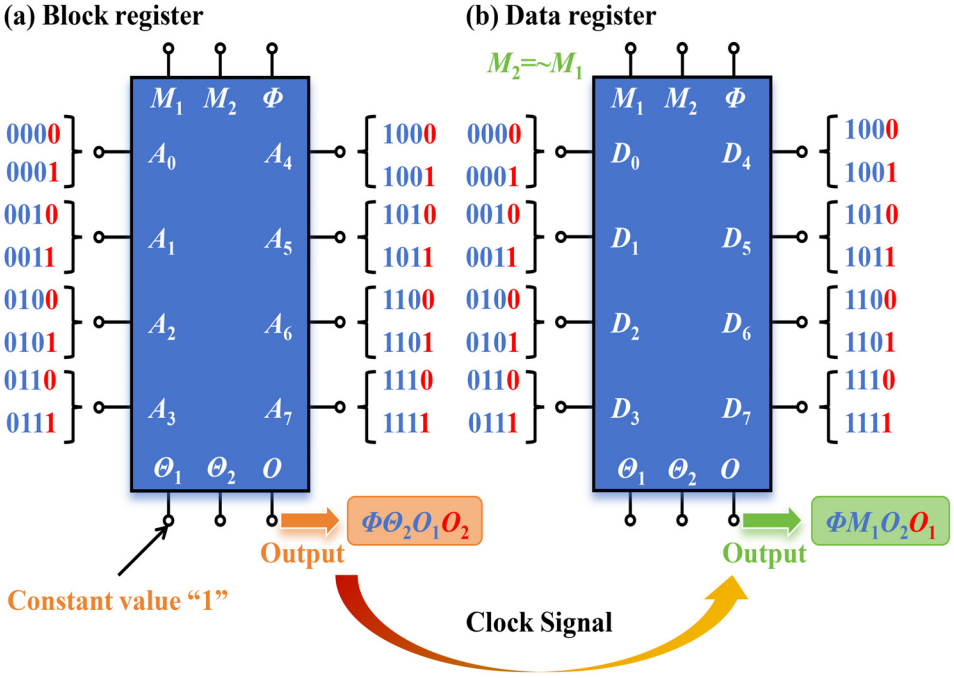


**FIG. 5.** Based on the clock signal, the LM implementation of block register and data register. (a) The input bits and output bits of the block register. (b) The input bits and output bits of the data register.

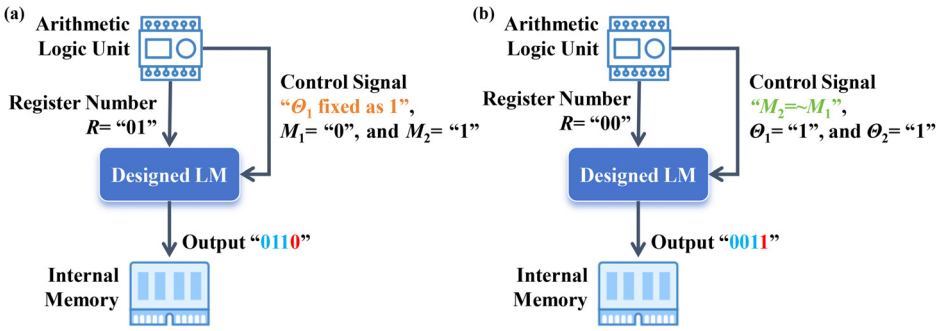


FIG. 6. Detailed data transmission processes from arithmetic logic unit to memory. (a) Output when LM works as a block register. (b) Output when LM works as a data register.

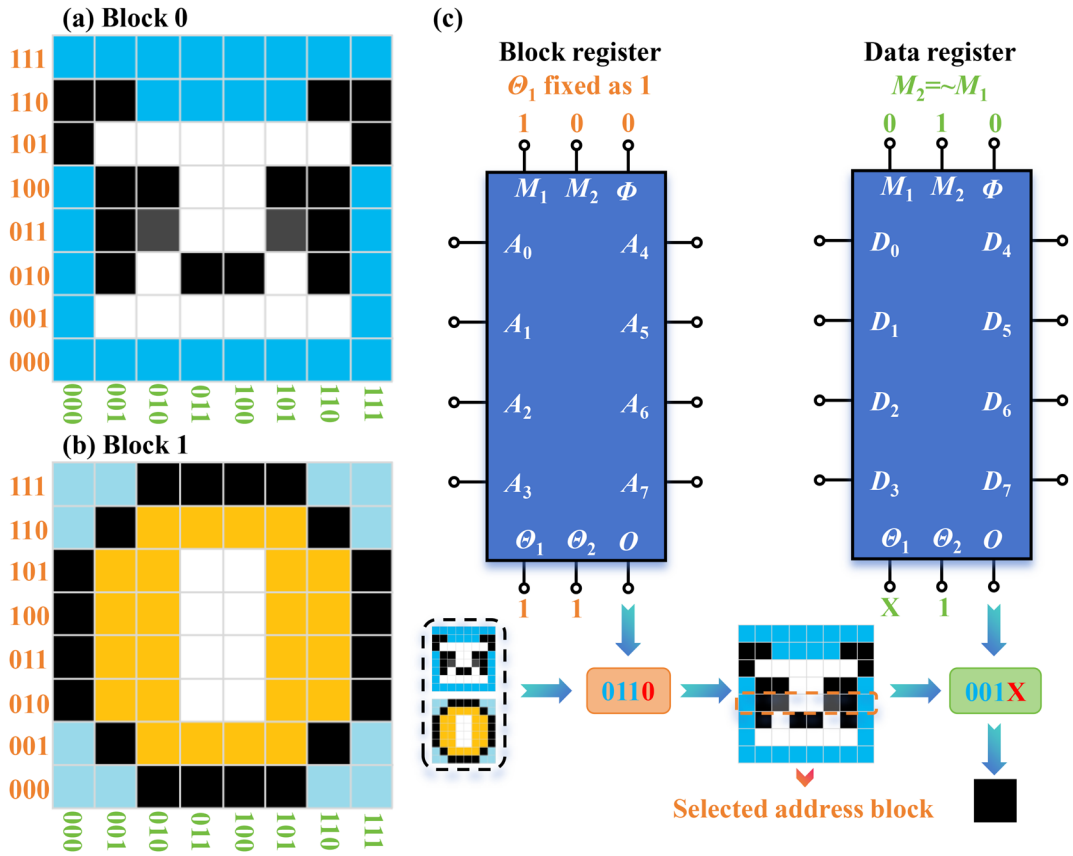


FIG. 7. The flow chart of register function implementation based on the LM. (a) Data stored at block 0. (b) Data stored at block 1. (c) The process of realizing real data register based on block register and data register controlled by a clock signal.

gates, this study advances the field by implementing a complete sequential logic device.

In summary, a CPA-enabled LM with advanced register functionality is presented. The proposed one-dimensional layered architecture (detailed preparation scheme in Sec. IX of the supplementary material) achieves dual electromagnetic wave selectivity in both frequency and angular domains within designated spectral ranges, enabled by dynamically tuning $\mu_1$, $\mu_2$, $\theta_1$, $\theta_2$, and $\Delta\varphi_{12}$. A systematic logic framework is established by defining input/output signal relationships, yielding two operational modes that govern the logical behavior of the LM. Under synchronized clock signal control, the system realizes 128-address data registration through the coordinated operation of dual-state registers. The block register is used to locate the block of data, and the function of the data register is data retrieval. This LM delivers high-accuracy computations with enhanced high SNR (9.5 dB). Through frequency and spatial reuse, this study enhances the complexity and performance of electromagnetic calculation in comparison with the reported OLDs. In addition, the LM also has

**TABLE V.** The performance of this work was compared with that of the published OLDs.

| References | *SNR* (dB) | Logic operation | Logic device | Output bit | LM | CPA |
|---|---|---|---|---|---|---|
| 24 | 4.5 | XOR and AND | Half-adder | 2 bit | × | × |
| 25 | 6.5 | NOT, NOR, OR, and AND | × | 1 bit | × | × |
| 26 | × | OR, NOR, XOR, and AND | × | 1 bit | × | × |
| 27 | 2.1 | AND, OR, XOR, NAND, NOR, XNOR, and NOT | × | 1 bit | × | × |
| 28 | 5.8 | NOT, NOR, and AND | × | 1 bit | × | × |
| 29 | × | NOT, AND, NAND, OR, NOR, XOR, and XNOR | × | 1 bit | √ | × |
| This work | 9.5 | AND and XNOR | Register | 8 bit | √ | √ |

certain advantages in terms of speed and energy consumption (a detailed comparison is in Sec. X of the supplementary material).

Although this work has achieved the function of register based on the LM, its scalability is an urgent problem to be solved. Moreover, the optical register model proposed in this work is based on the existing theory. Systematic research on the influence of defects on performance in actual preparation also urgently needs to be followed up. In addition, the improvement of the preparative technique and the development of materials science (search materials that can replace graphene), will also greatly enhance the practical application value of this work.

See the supplementary material for CPA realizing based on phase matching, S-parameter for multi-spatial angle domains, verification based on simulation software "High-Frequency Simulator Structure," error analysis, the detailed truth table for register function, clock signal definition, preparation methods, and the specific advantages in terms of speed and energy consumption.

This work was supported by the National College Students Innovation and Entrepreneurship Training Program (Grant No. 202410293018Z).

## AUTHOR DECLARATIONS

### Conflict of Interest

The authors have no conflicts to disclose.

### Author Contributions

**Jia-Hao Zou:** Funding acquisition (lead); Investigation (lead); Validation (lead); Writing – original draft (lead). **Jun-Yang Sui:** Formal analysis (lead); Resources (lead); Software (lead); Visualization (lead). **Hai-Feng Zhang:** Conceptualization (lead); Project administration (lead); Supervision (lead); Writing – review & editing (lead).

## DATA AVAILABILITY

The data that support the findings of this study are available from the corresponding author upon reasonable request.

## REFERENCES

[1]H. Xiong, Q. Yang, Y.-Z. Huang, J.-H. Deng, B.-X. Wang, and H.-Q. Zhang, ACS Appl. Mater. Interfaces **16**(44), 60189–60196 (2024).
[2]H. Xiong, Q. Yang, Y.-Z. Huang, X. Wang, Z. Yi, and H.-Q. Zhang, Appl. Phys. Lett. **125**(4), 043901 (2024).
[3]S. Fang, Z. Yang, Y. Tao, W. Lv, J. Jiang, D.-Q. Zhang, B.-X. Wang, G. Yang, and F.-Z. Shu, Opt. Laser Technol. **183**, 112345 (2025).
[4]B.-X. Wang, G. Duan, W. Lv, Y. Tao, H. Xiong, D.-Q. Zhang, G. Yang, and F.-Z. Shu, Nanoscale **15**(45), 18435–18446 (2023).
[5]L. He, F. Zhang, H. Zhang, L.-J. Kong, W. Zhang, X. Xu, and X. Zhang, ACS Photonics **9**(2), 597–604 (2022).
[6]C. A. Thraskias, E. N. Lallas, N. Neumann, L. Schares, B. J. Offrein, R. Henker, D. Plettemeier, F. Ellinger, J. Leuthold, and I. Tomkos, IEEE Commun. Surv. Tutorials **20**(4), 2758–2783 (2018).
[7]D. C. Tzarouchis, B. Edwards, and N. Engheta, Nat. Commun. **16**(1), 908 (2025).
[8]M. Manjappa, P. Pitchappa, N. Singh, N. Wang, N. I. Zheludev, C. Lee, and R. Singh, Nat. Commun. **9**(1), 4056 (2018).
[9]X. Ding, Z. Zhao, P. Xie, D. Cai, F. Meng, C. Wang, Q. Wu, J. Liu, S. N. Burokur, and G. Hu, Adv. Mater. **36**(9), 2308993 (2024).
[10]Z. Zhao, Y. Wang, X. Ding, H. Li, J. Fu, K. Zhang, S. N. Burokur, and Q. Wu, Photonics Res. **10**(2), 316–322 (2022).
[11]A. Bhattacharya, B. S. Chouhan, K. Sharma, S. M. Halawani, A. Ahmad, and G. Kumar, Sci. Rep. **14**(1), 8721 (2024).
[12]H. Zeng, X. Cong, H. Zhang, S. Gong, T. Zhou, L. Wang, H. Cao, H. Liang, S. Liang, S. Wang, F. Lan, X. Wang, Z. Yang, Y. Zhang, and T. J. Cui, Sci. Adv. **10**(49), eadr1448 (2024).
[13]J. H. Zou, J. Y. Sui, and H. F. Zhang, Phys. Fluids **37**(1), 017169 (2025).
[14]J. Chen, S. Hu, S. Zhu, and T. Li, Interdiscip. Mater. **2**(1), 5–29 (2023).
[15]Y. D. Chong, L. Ge, H. Cao, and A. D. Stone, Phys. Rev. Lett. **105**(5), 053901 (2010).
[16]D. Yan, R. Mei, M. Li, Z. Ma, Z. H. Hang, and J. Luo, Nanophotonics **12**(22), 4195–4204 (2023).
[17]I. H. Malitson, J. Opt. Soc. Am. **55**(10), 1205–1209 (1965).
[18]T. Amotchkina, M. Trubetskov, D. Hahner, and V. Pervak, Appl. Opt. **59**(5), A40–A47 (2020).
[19]G. W. Hanson, J. Appl. Phys. **103**(6), 064302 (2008).
[20]X. K. Kong, S. B. Liu, H.-F. Zhang, S.-Y. Wang, B.-R. Bian, and Y. Dai, IEEE J. Sel. Top. Quantum Electron. **19**(1), 8401407–8401407 (2013).
[21]W. Zhu, F. Xiao, M. Kang, and M. Premaratne, Appl. Phys. Lett. **108**(12), 121901 (2016).
[22]J. Ma, S. Zhang, H. Li, N. Zhao, and V. C. M. Leung, IEEE Trans. Wireless Commun. **17**(3), 1907–1922 (2018).
[23]D. H. Johnson, Scholarpedia **1**, 2088 (2006).
[24]Y. Pugachov, M. Gulitski, O. Mizrahi, and D. Malka, Symmetry **15**(5), 1063 (2023).
[25]A. Ghadi and B. Darzi, Opt. Laser Technol. **157**, 108651 (2023).
[26]Y. Chen, Z. Huang, J. Huang, L. Shao, F. Gao, X. Chen, S. N. Khisro, and Y. Zhang, Appl. Phys. Lett. **122**(3), 033501 (2023).
[27]J. Jot Singh, D. Dhawan, and N. Gupta, Opt. Laser Technol. **165**, 109624 (2023).
[28]S. Soma, S. K. C. Gowre, M. V. Sonth, B. Gadgay, and B. Jyoti, Opt. Quantum Electron. **55**(4), 340 (2023).
[29]H. Yang, J. Yang, and J. Wu, Results Phys. **58**, 107544 (2024).